Earthquake Geotechnical Engineering for Protection and Development of Environment and Constructions – Silvestri & Moraci (Eds)
© 2019 Associazione Geotecnica Italiana, Rome, Italy, ISBN 978-0-367-14328-2

Numerical study about liquefaction of body of embankment considering unsaturated conditions

T. Matsumaru & T. Sato
Railway Technical Research Institute, Tokyo, Japan

ABSTRACT: In this paper, the numerical analysis focused on the liquefaction of the body of the embankment was performed with the three-phase (soil, water, and air) coupled analysis based on porous media theory. In this technique, the conventional constitutive model for describing the cyclic behavior of unsaturated soil was employed. From the numerical simulations about the shaking table test, it was revealed that the simulation could reproduce the experimental results well. Furthermore, the series of simulations indicated that the existing railway embankment could be deformed beyond the limitation of the settlement required in design.

1 INTRODUCTION

The 2011 off the Pacific coast of Tohoku earthquake caused significant damages of river dikes and road and railway embankments (Sasaki et al, 2012; Koseki et al, 2012). In this earthquake, several damages were caused due to the occurrence of the liquefaction in the body of the embankments. This kind of damages was also observed in the Kushiro-Oki earthquake in 1993 (Sasaki et al, 1994). However, the studies concerning this problem have not been conducted because the main reasons of the damages of embankments were the liquefaction of the foundation ground. After the 2011 Tohoku earthquake, a few numbers of experimental studies have been conducted using centrifuge shaking table tests (Okamura et al, 2012). The numerical studies have been also conducted focused on the river embankment (Uzuoka and Semba, 2014). In their numerical studies, they considered the unsaturated conditions because recent laboratory tests show the possibility of occurrence of liquefaction even in unsaturated conditions (e.g. Okamura and Soga, 2006). However, the validation of the numerical methods has not been confirmed.

In this paper, the numerical analysis focused on the liquefaction of the body of the embankment was performed with the three-phase (soil, water, and air) coupled analysis based on porous media theory (Uzuoka and Borja, 2012). In this technique, the conventional constitutive model for describing the cyclic behavior of unsaturated soil was employed (Matsumaru and Uzuoka, 2014). The simulation analysis of the shaking table tests was performed in order to validate the numerical technique. Furthermore, the series of simulations were conducted in order to check the liquefaction resistance of existing railway embankment.

2 NUMERICAL TECHNIQUE

2.1 *Density and stress of three-phase porous media*

The overall density of mixture ρ can be expressed as

$$\rho = \rho^s + \rho^w + \rho^a = (1-n)\rho^{sR} + n\left\{s^w\rho^{wR} + (1-s^w)\rho^{aR}\right\} \quad (1)$$

where ρ^{s}, ρ^{w} and ρ^{a} are the partial densities of soil skeleton, pore water and air respectively. ρ^{sR}, ρ^{wR} and ρ^{aR} are the real densities of each phase, n is the porosity and s^{w} is the degree of water saturation.

The skeleton stress which means the effective stress of unsaturated soil is expressed as:

$$\begin{aligned}\boldsymbol{\sigma} &= \boldsymbol{\sigma}^s + \boldsymbol{\sigma}^w + \boldsymbol{\sigma}^a = \boldsymbol{\sigma}' - p^a\mathbf{I} + s^w(p^a - p^w)\mathbf{I} \\ (-\boldsymbol{\sigma}') &= (-\boldsymbol{\sigma}) - p^a\mathbf{I} + s^w(p^a - p^w)\mathbf{I}\end{aligned} \tag{2}$$

where σ' is the skeleton stress tensor, p^{w} is the pore water pressure and p^{a} is the pore air pressure. These pressures are defined as positive in compression.

2.2 *Soil water characteristic curve*

The SWCC (soil water characteristic curve) is assumed as a logistic function derived by

$$s^w = \left(s_s^w - s_r^w\right)s_e^w + s_r^w \qquad s_e^w = \left\{1 + \exp\left(a_{\mathrm{lg}}p^c + b_{\mathrm{lg}}\right)\right\}^{-c_{\mathrm{lg}}} \tag{3}$$

where s_s^w is the saturated (maximum) degree of saturation, s_r^w is the residual (minimum) degree of saturation and s_e^w is the effective water saturation. The relationship between s_e^w and suction p^{c} is assumed as a logistic function with the material parameters a_{lg}, b_{lg} and c_{lg}. The logistic SWCC is a continuous function at $p^{\mathrm{c}} = 0$; therefore the convergence in the iterative numerical scheme can be achieved.

The permeability coefficient of water and air are assumed to be dependent on the effective water saturation as:

$$k^{ws} = k_s^w\left(s_e^w\right)^{\xi_k} \qquad k^{as} = k_s^a\left(1 - s_e^w\right)^{\eta_k} \tag{4}$$

where k_s^w is the saturated (maximum) coefficient of water permeability, k_s^a is the dry (maximum) coefficient of air permeability, ξ_{k} and η_{k} are the material parameters.

2.3 *Constitutive equation for skeleton stress*

A simplified constitutive model for saturated sandy soil is used for unsaturated soil with using a skeleton stress in place of an effective stress of saturated soil. Assuming that plastic deformation occurs only when the deviatoric stress ratio changes, the yield function is assumed as:

$$f = \sqrt{\frac{3}{2}}\|\boldsymbol{\eta} - \boldsymbol{\alpha}\| - k = 0 \tag{5}$$

where η is the stress ratio and k is the material parameter which defines the elastic region.

The kinematic hardening parameter (back stress) α, and its nonlinear evolution rule (Armstrong and Frederick, 1966) is assumed as:

$$\dot{\boldsymbol{\alpha}} = a\left(\frac{2}{3}b\dot{\mathbf{e}}^p - \alpha\dot{\varepsilon}_d^p\right) \qquad \dot{\varepsilon}_d^p = \|\dot{\mathbf{e}}^p\| \tag{6}$$

where a and b are the material parameters, and $\dot{\mathbf{e}}^p$ is the plastic deviatoric strain rate tensor.

Using the following equation, the hardening parameter α is reduced according to the value of the equivalent plastic strain $\varepsilon_d^{p(n)}$ which is reset when the direction of loading changes, assumed as:

$$\dot{\boldsymbol{\alpha}} = a\left(\frac{2}{3}b\dot{\mathbf{e}}^p - \alpha\dot{\varepsilon}_d^p\right) \qquad \dot{\varepsilon}_d^p = \|\dot{\mathbf{e}}^p\| \tag{7}$$

where a_0 is the initial value of the material parameter a, a_1 is the lower limit value of a and C_{f} is the parameter which controls the amount of the reduction a. In order to describe plastic strain rate more precisely, the non-associated flow rule was adopted, assumed as:

$$\dot{\boldsymbol{\varepsilon}}^p = \dot{\boldsymbol{\Lambda}}\frac{\partial g}{\partial \sigma} \qquad \dot{\boldsymbol{\Lambda}} = \dot{\lambda}_1\delta_{ij}\delta_{kl} + \dot{\lambda}_2\left(\delta_{ik}\delta_{jl} + \delta_{il}\delta_{jk}\right) \tag{8}$$

where $\dot{\lambda}_1$ and $\dot{\lambda}_2$ are the material parameters depending on the situations of stress and strain. From the equation (8), the plastic deviatoric strain rate and the plastic volumetric strain are derived as:

$$\dot{\mathbf{e}}^p = 2\dot{\lambda}_2 \frac{\partial g}{\partial \mathbf{s}} = \dot{\gamma}\frac{\partial g}{\partial \mathbf{s}} \quad \dot{\varepsilon}_v^p = \left(3\dot{\lambda}_1 + 2\dot{\lambda}_2\right)\frac{\partial g}{\partial p} = D\dot{\gamma}\frac{\partial g}{\partial p}$$
$$\dot{\gamma} = 2\dot{\lambda}_2 \qquad D = \frac{3\dot{\lambda}_1}{2\dot{\lambda}_2} + 1 \tag{9}$$

where $\dot{\gamma}$ is the hardening coefficient and D is the coefficient of dilatancy. In order to change the volumetric strain rate depending on the suction p^{c} of unsaturated soil, we propose an equation which describes the relationship between the coefficient of dilatancy and the suction p^{c}, assumed as:

$$\begin{aligned} D &= D_1 + (D_0 - D_1)\exp\left(-p^c/p^c_{ref}\right) && (p^c > 0) \\ D &= D_0 && (p^c \le 0) \end{aligned} \tag{10}$$

where D_0 is the initial value of the coefficient of dilatancy$D$, D_1 is the lower limit value of D and the p^c_{ref} is the parameter which controls the amount of the reduction of D. The equation (10) means that the plastic volumetric strain tends not to occur if the suction p^{c} is large.

With the non-associated flow rule, the plastic potential function is assumed as:

$$g = \sqrt{\frac{3}{2}}\|\boldsymbol{\eta} - \boldsymbol{\alpha}\| + M_m \ln\left(\frac{p'}{p'_a}\right) \tag{11}$$

where M_{m} is the critical state stress ratio, and p'_a is p' when $\|\eta - \alpha\| = 0$.

Finally the elastic bulk modules are assumed as:

$$K^e = -K^* p' \qquad G^e = -G^* p' \tag{12}$$

where K^e is the elastic bulk modulus, G^e is the elastic shear modulus, K^* and G^* are the dimensionless elastic modules, respectively.

2.4 *Constitutive equation for skeleton stress*

The governing equations are derived by Uzuoka and Borja (2012) with following assumptions. 1) The conditions are isothermal, 2) the soil particles are incompressible, 3) the mass exchange among phases can be neglected, and 4) the material time derivative of relative velocities and advection terms of pore fluids to the soil skeleton can be neglected.

The momentum balance equation of the overall three phase material is derived as:

$$\rho \mathbf{a}^s = \mathrm{div}[\boldsymbol{\sigma}' - \{s^w p^w + (1 - s^w)p^a\}\mathbf{I}] + \rho \mathbf{b} \tag{13}$$

where $\mathbf{a}^{\mathrm{s}}$ is the acceleration of solid skeleton and $\mathbf{b}$ is the gravity acceleration vector. The mass and momentum balance equations of the pore water and air are derived as:

$$\begin{aligned} &\left(\frac{ns^w\rho^{wR}}{K^w} - n\rho^{wR}c\right)\frac{D^s p^w}{Dt} + n\rho^{wR}c\frac{D^s p^a}{Dt} + s^w\rho^{wR}\mathrm{div}\mathbf{v}^s \\ &\quad + \mathrm{div}\left\{\frac{k^{ws}}{g}\left(-\mathrm{grad}p^w + \rho^{wR}\mathbf{b}^w - \rho^{wR}\mathbf{a}^s\right)\right\} = 0 \end{aligned} \tag{14}$$

$$\begin{aligned} &\left(\frac{n(1 - s^w)}{\Theta R} - n\rho^{aR}c\right)\frac{D^s p^a}{Dt} + n\rho^{aR}c\frac{D^s p^w}{Dt} + (1 - s^w)\rho^{aR}\mathrm{div}\,\mathbf{v}^s \\ &\quad + \mathrm{div}\left\{\frac{k^{as}}{g}\left(-\mathrm{grad}\,p^a + \rho^{aR}\mathbf{b}^a - \rho^{aR}\mathbf{a}^s\right)\right\} = 0 \end{aligned} \tag{15}$$

where K^{w} is the bulk modulus of the pore water, c is the specific water capacity, Θ is the absolute temperature, R is the specific gas constant of air, $\mathbf{v}^s$ is the velocity of soil skeleton and g is the acceleration of gravity.

Weak forms of the equations (13)–(15) are implemented in a finite element formulation. Newmark implicit scheme is used for time integration. The primary variables are the second-order material time derivative of displacement of soil skeleton $\mathbf{a}^s$, pore water pressure $\ddot{p}^w$ and pore air pressure$\ddot{p}^a$. The weak forms are linearized and solved by Newton-Raphson method iteratively at each time step.

In the finite element formulation, Galerkin method and isoparametric 8-node elements are used. The soil skeleton displacement and the fluid pressures are approximated at 8 nodes and 4 nodes respectively to avoid volumetric locking.

3 ANALYSIS OF SHAKING TABLE

3.1 *Outline of shaking table test*

Figure 1 shows the experimental model of the embankment and ground. The dimension of the embankment was 40 cm in height, 30 cm in width at the top, and 1: 1.5 in gradient of slope. The embedded zone with 15 cm in height was prepared after the ground was prepared, in order to reproduce the condition where the embankment settled due to consolidation.

The material of the embankment was Inagi sand, whose particle density G_s was 2.723; 50 % diameter on the grain size diagram D_{50}, 0.134 mm; the uniformity coefficient U_c, 9.29; the fine fraction content F_c, 23.6 %; and the maximum dry density, 1.517 g/cm^3. The embankment was prepared so that the dry density and the water content would be 1.108 g/cm^3 and about 13 % respectively. The dry density of the embankment was set much smaller than the maximum dry density, in order to make the seepage easy and to avoid setting the cohesion excessive taking the similarity law into consideration. On the other hand, the ground was constructed also using Inagi sand except the bottom layer, with efficient compaction for avoiding the occurrence of settlement and liquefaction.

The measurement included the degree of saturation, acceleration, pore water pressure and displacement for making dynamic behavior of the embankment clear. Furthermore, we photographed reference points in the embankment with a high-speed camera and analyzed the obtained data in order to estimate a deformation mode.

Figure 2 shows the time history of the input motion. The wave used for shaking was a sinusoidal wave of 3 Hz in the frequency and 200 gal in the amplitude. The motion continued about 120 seconds. Figure 1 shows the example of the input motion.

Figure 3 shows the deformed embankment at 70 sec. and at the end of shaking. Affected by the shaking, the clack appeared at the top and the dissipation of pore water was observed at the toe. At the end of the shaking, the embankment settled and showed the flat shape due to the boundaries of the shaking box. On the other hand, the embedded zone showed small deformation and would not be liquefied, judged from the movement of the reference points.

3.2 *Analytical conditions*

Figure 4 shows the finite element modeling of the embankment and the ground. The embankment was divided in square eight-node elements. The soil displacement at the bottom boundary was fixed in all directions and the lateral boundaries were vertical rollers. The bottom and lateral boundaries were impermeable and the part of the surface on the embankment was permeable with zero water pressure. Regarding pore air pressure, the bottom and side boundaries were impermeable, while air drainage was allowed at the surface of the ground and the embankment.

The material parameters of the constitutive models were determined through the calibration of the unsaturated cyclic triaxial tests with the embankment materials (Matsumaru and

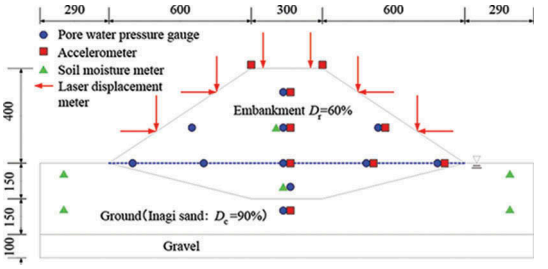

Figure 1. Experimental model.

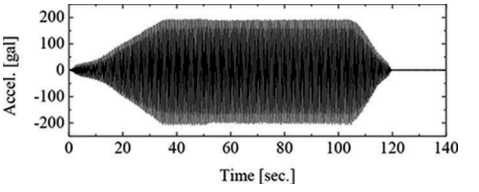

Figure 2. Time history of input motion.

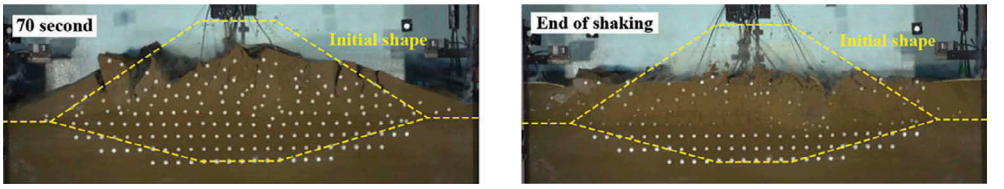

Figure 3. Photographs of deformed embankment.

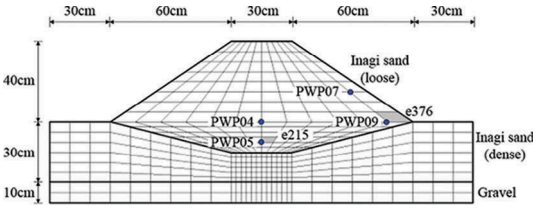

Figure 4. Finite element model.

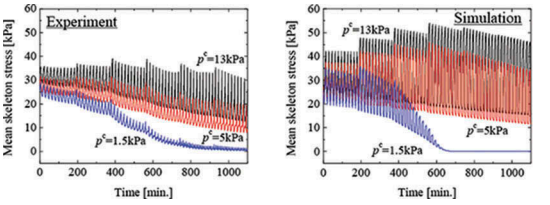

Figure 5. Results of triaxial tests and simulations.

Uzuoka, 2014). The degree of water saturation was from about 43 % to 79 % according to the air pressure controlled during the isotropic consolidation process. The pore water pressure was almost zero after the consolidation and the pore air pressure increased with the decrease in water saturation. The net stress was about 25 kPa for all specimens and the mean skeleton stress varied with the initial suction p^c dependent on initial water saturation. The cyclic shear was applied to the specimen under undrained air and water conditions. The input axial strain has eleven cycles of the triangular waves with multi step amplitudes of 0.1, 0.2, 0.5, 1.0, 1.5, and 2.0. The frequency of the sinusoidal wave was 0.001 Hz. This loading rate was slow enough to achieve an equilibrium condition between air and water pressure.

Figure 5 shows the time histories of the mean skeleton stress obtained by experiments and simulations of the cyclic triaxial tests. The mean skeleton stress attained zero in the case of p^c=1.5kPa which means that the specimen was liquefied completely. On the other hand, the graphs of the cases of p^c=13kPa and p^c=5kPa, showed different results, which means that the strength and stiffness was maintained during the cyclic shear. In the simulated results, the model well reproduced the overall tendency of the test results of each case. The determined parameters for the elasto-plastic constitutive model were applicable to the prediction of the responses of unsaturated cyclic loading of the materials for the embankment.

For the dynamic analysis, the coefficients in Newmark implicit time integration were 0.6 and 0.3025. The time increment was 0.001 second for all cases. In the dynamic analyses, the viscos damping of the solid skeleton was considered. The damping coefficient was 0.001.

3.3 *Results and discussions*

Figure 6 shows the time histories of the excess pore water pressure (EPWP) at PWP04, 05, 07 and 09. The simulation reproduced the time and the amount of the increase of EPWP well except that at PWP09. At PWP09, the time of the increase of EPWP obtained by the simulation was earlier and the amount was smaller than those of the experiment.

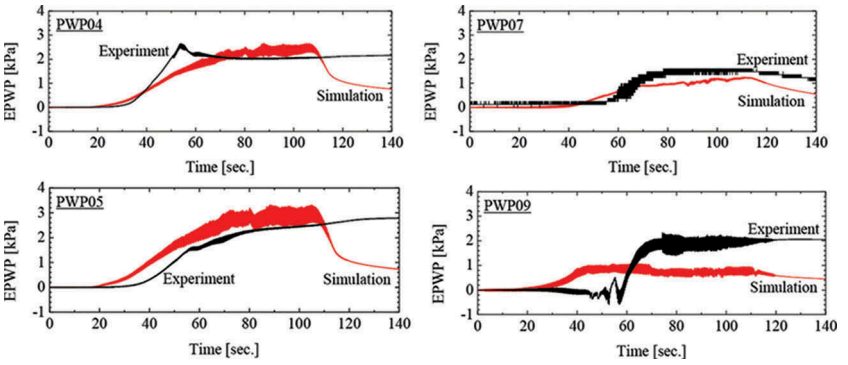

Figure 6. Time histories of excess pore water pressure.

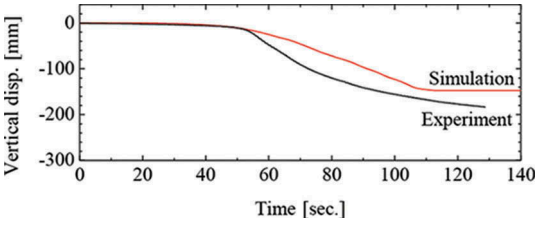

Figure 7. Time history of vertical displacement.

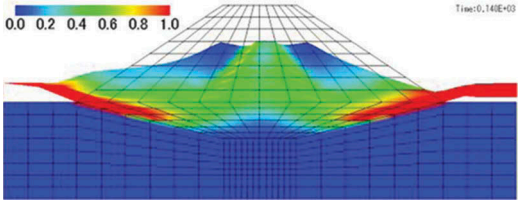

Figure 8. Distribution of accumulated strain.

Figure 7 shows the time histories of the vertical displacement at the top of the embankment. The simulation reproduced the settlement of the embankment well compared to the experimental result. Figure 8 shows the deformed shape of the embankment and the distributions of the accumulated strain after the end of the shaking. A large strain appeared at the toe of the embankment and the circular slip surface appeared from the toe to the top of the embankment. This would cause the large settlement of the embankment. The value of the strain would exceed the limitation of the small strain theory adopted in this simulation, so it was required to use the formula based on the finite deformation theory or the particle material method which can describe the large deformation of the embankment.

Figure 9 shows the distributions of the value of the mean skeleton stress reduction ratio (MSSRR) at 100 second. At the toe of the embankment, the MSSRR reached 1.0. This would cause the large strain at the toe as shown in Figure 8. On the other hand, liquefaction did not occur at the center of the embankment where the PWP04 and 05 were located. In order to make this difference clear, Figure 10 shows the stress pass at e376 and e215. At e376, the mean skeleton stress reached zero during shaking, so this element would be liquefied. On the other hand, the element at e215, the initial stress state was close to the critical state line and reached this line during shaking. At this element, not liquefaction but shear failure would occur.

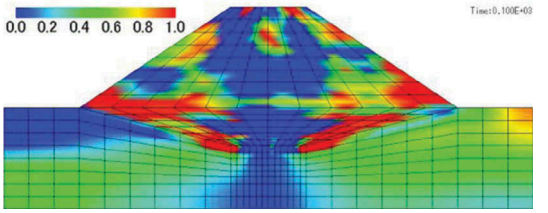

Figure 9. Distributions of MSSRR.

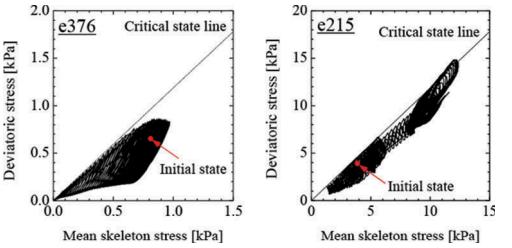

Figure 10. Stress pass of elements.

4 ANALYSIS ABOUT EXISTING RAILWAY EMBANKMENT

4.1 *Analytical discussions*

Figure 11 shows the analytical model used in simulations. The dimension of the embankment was 6 m in height, 10 m in width at the top, and 1: 1.5 in gradient of slope. In this analysis, equivalent displacement boundary condition at the both side boundaries was introduced in order to describe the deformation of the free ground.

Figure 12 shows the time histories of input motion. This motion is used for seismic design of railway structures (Railway Technical Reseach Insutitute, 2012).

Table 1 shows the analytical cases. Case 1 is the basic case for comparison with other cases. For the embankment material, the material which satisfies R_{l20}=0.2 was considered except Case 2 in order to consider a not-well compacted embankment. R_{l20} is the cyclic shear stress ratio which causes 5 % in double amplitude of the shear strain, by twenty cycles of loading. In Case 2, the material which satisfies R_{l20}=0.5 is assumed for the consideration of the well compacted embankment. In Case 3, 4 and 5, the water level, the saturated permeability coefficient and the depth of embedded zone is changed.

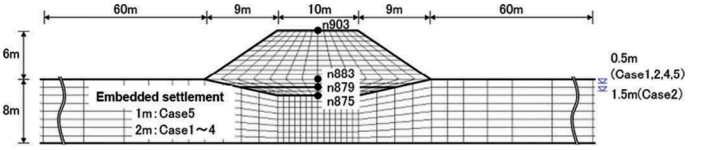

Figure 11. Finite element model.

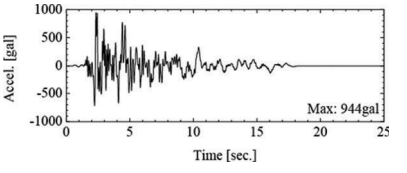

Figure 12. Time history of motion.

Table 1. Cases of simulations.

	Case1	Case2	Case3	Case4	Case5
Liquefaction Resistance R_{l20}	0.2	0.5	0.2	0.2	0.2
Water level [m]	-0.5	-0.5	-1.5	-0.5	-0.5
Permeability coefficient [m/s]	1.0×10^{-4}	1.0×10^{-4}	1.0×10^{-4}	1.0×10^{-4}	1.0×10^{-4}
Depth of embedded zone [m]	2.0	2.0	2.0	2.0	1.0

4.2 *Results and discussions*

Figure 13 shows the settlement of the embankment after the earthquake. The settlement was divided in three components; compression of the ground, the embedded zone and the embankment body, calculated as the difference of each nodal displacement as show in Figure 11. In the seismic design of railway embankments, the design is usually conducted so that the settlement of the embankment is smaller than 500 mm. Except Case 2, the settlement for each case exceeded this limitation. Compared to the result of Case 1, the settlement was largely evaluated in the case of higher water level, lower permeability coefficient and deeper embedded zone. On the other hand, the settlement in Case 2 was limited, so the increase of the resistance of liquefaction by well-compaction is important for avoiding the occurrence of the liquefaction of the embankment body.

In order to show the differences of the behaviors of the embankment, Figure 14 shows the distributions of MSSRR at 5 second and the accumulated strain after the earthquake in Case 1 and Case 4. Compared to the result in Case 1, liquefaction occurred at the embedded zone widely in Case 4. Affected by this, large strain occurred especially at the embedded zone and the strain in the embankment body in unsaturated conditions became larger. This would cause the larger settlement of the embankment in Case 4.

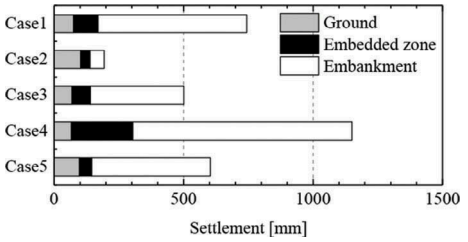

Figure 13. Settlement of embankment after earthquake.

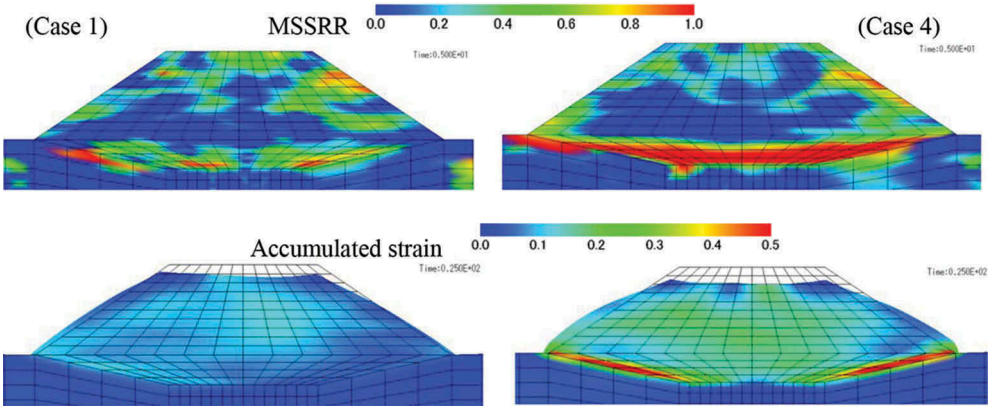

Figure 14. Distributions of MSSRR and accumulated strain.

5 CONCLUSIONS

In order to validate the numerical technique for the problem of liquefaction of the body of the embankment, numerical analysis with the three-phase (soil, water, and air) coupled analysis based on porous media theory were conducted for the reproduction of the shaking table tests. Furthermore, series of simulations were performed in order to show the liquefaction resistance for the existing railway embankment. As a result, we arrived to the following conclusions:

1. Numerical analyses could reproduce well the increase of the pore water pressure and showed good agreement with the deformation obtained in the experiments. From the point of view of the MSSRR in the simulation, liquefaction occurred even in the unsaturated regions. On the other hand, the embedded zone did not show the occurrence of liquefaction because the mean skeleton stress did not reach zero.
2. From the series of the simulations focused on the existing railway embankment, it was suggested that the severe settlement would occur if the liquefaction resistance is not enough. The value of the settlement was affected also by the height of the water level, the permeability of the embankment material, and the depth of the embedded zone.

REFERENCES

Armstrong, P. J. and Frederick, C. O. 1966. *A Mathematical Representation of the Multiaxial Bauschinger Effect*, Technical report C. E. G. B. Report RD/B/N731, Berkeley Nuclear Laboratories.

Koseki, J., Koda, M., Matsuo, S., Takasaki, H. and Fujiwara, T. 2012. Damage to railway earth structures and foundations caused by the 2011 off the Pacific Coast of Tohoku Earthquake, *Soils and Foundations*, 52(5): 872–889.

Matsumaru, T. and Uzuoka, R. 2014. Three-phase coupled analysis of unsaturated embankment subjected to rainfall infiltration and seismic motion, *Unsaturated Soils: Research & Applications*, 597–604.

Okamura, M. and Soga, Y. 2006. Effects of pore fluid compressibility on liquefaction resistance of partially saturated sand, *Soils and Foundations*, 46(4): 703–708.

Railway Technical Research Institute. 2012. *The Design Standards for Railway Structures and Commentary (Seismic Design), supervised by Ministry of Land*, Infrastructure and Transport, Maruzen (in Japanese).

Sasaki, Y., Oshiki, H., Nishikawa, J. 1993. Embankment failure caused by the Kushiro-Oki earthquake of January 15, *Session Publication during the 13th ICSMGE, Delhi*, 61–68.

Sasaki, Y., Towhata, I., Miyamoto, K., Shirato, M., Narita, A., Sasaki, T. and Sako, S. 2012. Reconnaissance report on damage in and around river levees caused by the 2011 off the Pacific coast of Tohoku earthquake, *Soils and Foundations*, 52(5): 1016–1032.

Uzuoka, R. and Borja, R. I. 2012. Dynamics of unsaturated poroelastic solids at finite strain, *International Journal for Numerical and Analytical Methods in Geomechanics*, 36: 1535–1573.

Uzuoka, R. and Semba, K. 2012. Numerical analysis of liquefaction in a river levee on soft cohesive ground, *Journal of Disaster Research*, 7(6): 711–717.